

Top of the Atmosphere Reflected Shortwave Radiative Fluxes from GOES-R

Rachel T. Pinker¹, Yingtao Ma¹, Wen. Chen¹, Istvan Laszlo², Hongqing Liu³,
Hye-Yun Kim³ and Jamie Daniels²

¹ Department of Atmospheric and Oceanic Science, University of Maryland, College Park, MD

² NOAA NESDIS Center for Satellite Applications and Research, College Park, MD

³I.M. Systems Group, Inc., Rockville, MD

Correspondence to: Rachel T. Pinker (pinker@atmos.umd.edu)

Abstract. Under the GOES-R activity, new algorithms are being developed at the National Oceanic and Atmospheric Administration (NOAA)/Center for Satellite Applications and Research (STAR) to derive surface and Top of the Atmosphere (TOA) shortwave (SW) radiative fluxes from the Advanced Baseline Imager (ABI), the primary instrument on GOES-R. This paper describes a support effort in the development and evaluation of the ABI instrument capabilities to derive such fluxes. Specifically, scene dependent narrow-to-broadband (NTB) transformations are developed to facilitate the use of observations from ABI at the TOA. Simulations of NTB transformations have been performed with MODTRAN4.3 using an updated selection of atmospheric profiles and implemented with the final ABI specifications. These are combined with Angular Distribution Models (ADMs), which are a synergy of ADMs from the Clouds and the Earth's Radiant Energy System (CERES) and from simulations. Surface condition at the scale of the ABI products as needed to compute the TOA radiative fluxes come from the International Geosphere-Biosphere Programme (IGBP). Land classification at 1/6 ° resolution for 18 surface types are converted to the ABI 2-km grid over the (CONTiguous States of the United States) (CONUS) and subsequently re-grouped to 12 IGBP types to match the classification of the CERES ADMs. In the simulations, default information on aerosols and clouds is based on the ones used in MODTRAN.

27 Comparison of derived fluxes at the TOA is made with those from CERES and the level of agreement
28 for both clear and cloudy conditions is documented. Possible reasons for differences are discussed. The
29 product is archived and can be downloaded from the NOAA Comprehensive Large Array-data
30 Stewardship System (CLASS).

31

32 **Introduction**

33

34 One of the objectives at NOAA/STAR in respect to the utilization of observations from the Advanced
35 Baseline Imager (ABI) is to be able to derive shortwave ($SW\downarrow$) radiative fluxes at the surface. To get to
36 the surface $SW\downarrow$ from TOA satellite observations, there are two generic approaches: 1) the direct approach
37 and 2) the indirect approach. In the direct approach one uses all the necessary information needed for
38 deriving the surface fluxes (some of which can be derived from satellites). Implementation of such an
39 approach is feasible, for instance, with observations from MODIS which has a long history of product
40 availability and evaluation. Examples are illustrated in Wang and Pinker (2009), Niu and Pinker, (2015),
41 Ma et al. (2016), Pinker et al. (2018), Pinker et al., (2017a), Pinker et al. (2017b). GOES-R is a new
42 instrument and as yet, similar information to the one from MODIS is not available. Therefore, the indirect
43 approach is used where one starts from satellite observations at the TOA and models the atmosphere and
44 surface with best available information (which does not have to be based on ABI). Examples of such an
45 approach are discussed in Pinker, Zhang and Dutton (2005), Ma and Pinker (2012) and Zhang et al.
46 (2019). The “indirect path method” is used at the Center for Satellite Applications and Research (STAR)
47 (Laszlo et al., 2020) for deriving $SW\downarrow$ radiative fluxes from satellite observations; it requires knowledge
48 of the SW broadband (0.2 – 4.0 μm) top of the atmosphere (TOA) albedo. The Advanced Baseline Imager
49 (ABI) observations onboard of the NOAA GOES-R series of satellites provide reflectance in six narrow
50 bands in the shortwave spectrum (**Table 1**); these must be first transformed into broadband reflectance
51 (the NTB conversion), and the broadband reflectance must be transformed into a broadband albedo (the
52 ADM conversion). During the pre-launch activity NTB transformations were developed based on
53 theoretical radiative transfer simulations with MODTRAN-3.7 and 14 land use classifications from the

54 International Geosphere-Biosphere Programme (*IGBP*) (Hansen et al., 2010). They were augmented with
55 ADMs from (CERES) observed ADMs (Loeb et al., 2003) and theoretical simulations (Niu and Pinker,
56 2011) to compute TOA fluxes. The resulting NTB transformations and ADMs have been tested using
57 proxy data and simulated ABI data. The proxy instruments used in these early simulations include the
58 GOES-8 satellite, the Advanced Very-High Resolution Radiometer (AVHRR) sensor on the Polar
59 Orbiting satellites, the Spinning Enhanced Visible Infra-Red Imager (SEVIRI) sensor on the European
60 METEOSAT Second Generation (MSG) satellites, and the Moderate Resolution Imaging
61 Spectroradiometer (MODIS) instrument on the NASA Terra and Aqua Polar Orbiting satellites (Pinker
62 et al., 2021, unpublished). For each of these satellites, the evaluation of the methodologies was done
63 differently; some results were evaluated against ground observations while others, against TOA
64 information from CERES as well as from the (ESA) Geostationary Earth Radiation Budget (GERB)
65 satellite (Harries et al., 2005). The results obtained provided an insight on the expected performance of
66 the new ABI sensor. Those procedures have been subsequently updated and applied to the new ABI
67 instrument once it was built and fully characterized.

68 This is a first paper that describes the development of a methodology to derive TOA SW fluxes from the
69 Advanced Baseline Imager onboard the NOAA GOES-R series of geostationary satellites that are used at
70 NOAA STAR as a starting point for deriving surface SW_↓ fluxes. Evaluation of the methodology against
71 best available estimates of TOA fluxes was also done. The TOA reflected SW flux is produced at NOAA
72 together with the surface SW_↓ flux and is archived at the NOAA Comprehensive Large Array-data
73 Stewardship System (CLASS) at avl.class.noaa.gov. While the TOA reflected SW flux is a product on its
74 own right, it is also a prerequisite to deriving the SW_↓ surface flux; as such, versions for TOA and surface
75 have the same labeling. The methodology will be presented in section 2, data used are described in section
76 3, results in section 4 and a summary and discussion in section 5.

77

78

79

80

81 2. Methodology

82

83 The following two flowcharts (**Figs. 1 and 2**) describe the necessary steps to derive the NTB
84 transformations and the ADMs. Details on these two steps will follow.

85 The TOA narrowband and broadband reflectance can be calculated from the spectral radiances
86 simulated from MODTRAN 4.3 and the response functions of the satellite sensor as shown in equations
87 (1) and (2):

$$88 \quad \rho_{nb}(\theta_0, \theta, \phi) = \frac{\pi \int_{\lambda_1}^{\lambda_2} I(\lambda, \theta_0, \theta, \phi) G(\lambda) d\lambda}{\int_{\lambda_1}^{\lambda_2} \cos(\theta_0) S_0(\lambda) G(\lambda) d\lambda} \quad (1)$$

$$89 \quad \rho_{bb}(\theta_0, \theta, \phi) = \frac{\pi \int_{0.2\mu m}^{4\mu m} I(\lambda, \theta_0, \theta, \phi) d\lambda}{\int_{0.2\mu m}^{4\mu m} \cos(\theta_0) S_0(\lambda) d\lambda} \quad (2)$$

90

91 Where:

92 ρ_{nb} : is narrowband reflectance;

93 ρ_{bb} : is broadband reflectance;

94 θ_0 : solar zenith angle;

95 θ : view (satellite) zenith angle; ϕ : relative azimuth angle;

96 I_λ : reflected spectral radiance; $S_0(\lambda)$: solar spectral irradiance;

97 G_λ : spectral response functions of satellite sensors; λ_1 and λ_2 are the spectral limits of the sensor spectral

98 band. This approach is widely used in the scientific community as also implemented in the work of Loeb

99 et al (2005), Wielicki et al. (2008), Su et al. (2015) and Akkermans et al. (2020).

100 As stated previously, the ADMs from CERES-based observations (Loeb et al., 2005; Kato et al. 2015)
 101 were augmented with theoretical simulations (Niu and Pinker, 2011) to compute TOA fluxes. This was
 102 done since CERES observations at that time were under-sampled at higher latitudes.
 103 The combined ADMs are developed for each angular bin by weighting the modeled and CERES ADMs
 104 based on the number of samples used to derive the ADMs of each type (Niu et al., 2011). Specifically:

$$\bar{R}(\theta_0, \theta, \phi) = \frac{1}{m+n} (m \times R_{CERES}(\theta_0, \theta, \phi) + n \times R_s(\theta_0, \theta, \phi)) \quad (3)$$

106 $\bar{R}(\theta_0, \theta, \phi)$: averaged ADMs at each angular bin;

107 R_{CERES} : anisotropic factor from CERES ADMs;

108 R_s : anisotropic factor from simulated ADMs;

109 m and n : observation numbers at angular bins for CERES and simulated ADMs.

110

111 **2.1 Selection of Atmospheric profiles for simulations**

112

113 We have selected 100 atmospheric profiles covering the globe and the seasons as input for simulations
 114 with MODTRAN4.3. The atmospheric profiles at each pressure level include temperature, water vapor
 115 and ozone. Each season includes 25 profiles. A tool was developed to select profiles from a Training Data
 116 set known as SeeBor Version 5.0 (https://cimss.ssec.wisc.edu/training_data/) (Borbas et.al. 2005).
 117 Originally it consisted of 15704 global profiles of temperature, moisture, and ozone at 101 pressure levels
 118 for clear sky conditions. The profiles are taken from NOAA-88, and the European Centre for Medium-
 119 Range Weather Forecasts (ECMWF) 60L training set, TIGR-3, ozone-sondes from 8 NOAA Climate
 120 Monitoring and Diagnostics Laboratory (CMDL) sites, and radiosondes from the Sahara Desert during
 121 2004. A technique to extend the temperature, moisture, and ozone profiles above the level of existing data

122 was also implemented by the providers (University of Wisconsin-Madison, Space Science and
123 Engineering Center, Cooperative Institute for Meteorological Satellite Studies (CIMSS). **Fig. 3** shows the
124 location of the selected profiles.

125 The SeeBor profiles are clear sky profiles. The top of the profiles is at 0.005 mb which is about 82.6 km.
126 We did an experiment to check the impact of reducing the number of levels for a profile (initially, we
127 have used only 40 levels). In the experiment computed were radiances from profiles with 50 levels as
128 well as radiances from profiles with 98 Levels. The difference between the two radiances (50 lev-98 lev)
129 were below 5 % reaching 15 % around 2.5 μm . In the experiment we used the odd number levels starting
130 from surface (plus the highest level) to reduce the number of profile levels. Based on these experiments
131 we have opted to keep all 98 profile levels.

132 The surface variables we have used are from MODIS and include surface skin temperature, 2 m
133 temperature, land/sea mask, and albedo. We have conducted a thorough investigation how the selected
134 profiles represent the entire sample of 15704 profiles. An example showing the comparison of
135 temperature, humidity and ozone profiles is shown in **Fig. 4**. As seen, there is a positive bias in the selected
136 profile of temperature due to their higher concentration at the lower latitudes. A positive bias can be found
137 at the lower levels while a negative bias is seen above 1 mb. Since our domain of study is in such latitudes
138 this selection should not have adverse effects on the simulations performed.

139

140 **2.2 Surface conditions**

141

142 Surface condition is one of the primary inputs into the MODTRAN simulations. The International
143 Geosphere-Biosphere Programme (IGBP) land classification is used as a source (Hansen et al., 2010;
144 Loveland et al., 2010). The dataset is at 1/6-degree resolution and includes 18 surface types. We have
145 converted the 1/6° (~18.5 km) resolution to the ABI 2-km grid using the nearest grid method (**Fig. 5**). The
146 surface type is fixed in time. The method for cloudy sky uses 4 surface types; these are also derived from
147 12 IGBP types (**Table 2**).

148

149 2.3 Clear and cloudy sky simulations

150

151 Under clear sky, scattering from aerosols is important. We have included 6 aerosol types (**Table 3**) to
152 cover a range of possible conditions under clear sky. Aerosol models are selected based on the type of
153 extinction and a default meteorological range for the boundary-layer aerosol models as listed below:

154 Aerosol Type 1: Rural extinction, visibility = 23 km

155 Aerosol Type 4: Maritime extinction, visibility = 23 km

156 Aerosol Type 5: Urban extinction, visibility = 5 km

157 Aerosol Type 6: Tropospheric extinction, visibility = 50 km

158 Aerosol Type 8: Advective Fog extinction, visibility = 0.2 km

159 Aerosol Type 10: Desert extinction for default wind conditions

160 For the 6 aerosol types, the total number of MODTRAN simulations for each surface type is 462,000. It
161 is obtained as follows: 6 aerosol types x 100 profiles x 770 angles.

162 When performing NTB simulations, we use all 6 types of aerosols. The Rural, Ocean, Urban and Fog
163 aerosols are distributed in the lower 0-2 km region. Tropospheric aerosol is distributed from 0 to 10 km
164 tropopause. The Rural, Ocean, Urban and Tropospheric aerosol optical properties have Relative Humidity
165 (RH) dependency. The Single Scattering Albedo (SSA) is given on 4 RH grids (0, 70, 80, 99) on a spectral
166 grid of 788 points ranging from 0.2 to 300 microns.

167 Simulations were performed for ABI for all the cloud cases described in **Table 3**. To merge cloud layers
168 with atmospheric profiles we have followed the procedure as described in *Berk et al.* (1985, 1998),
169 namely: “Cloud profiles are merged with the other atmospheric profiles (pressure, temperature, molecular
170 constituent, and aerosol) by combining and/or adding new layer boundaries. Any cloud layer boundary
171 within half a meter of an atmospheric boundary layer is translated to make the layer altitudes coincide;
172 new atmospheric layer boundaries are defined to accommodate the additional cloud layer boundaries.”
173 100% relative humidity is assumed within the cloud layers (default).

174

175

176 **2.4 Selection of angles**

177

178 The total number of angles used in the simulations is given in **Table 4**. The selected spectral grids for
179 solar zenith angles, satellite view angles and relative azimuth angles are at Gaussian quadrature points,
180 plus 0° to solar zenith angles (sza) and satellite viewing angles (vza) and 0° and 180° (forward and
181 backward view) to the satellite relative azimuth angles. Solar angle and satellite view angle are referenced
182 to target or surface for satellite simulation with 0° meaning looking up (zenith). Relative azimuth angle is
183 defined as when the relative azimuth angle equals 180° , the sun is in front of observer.

184 The definitions of solar zenith angle and azimuth angle in this table corresponds to the definitions of
185 MODTRAN but that is not the case for the satellite zenith angle. MODTRAN uses nadir angle as 180° -
186 satellite zenith angle, ignoring spherical geometry.

187

188 **2.5 Selection of optimal computational scheme**

189

190 MODTRAN4.3 provides three multiple scattering models (Isaacs, DISORT, and Scaled Isaacs) and three
191 band models at resolutions (1 cm^{-1} , 5 cm^{-1} , and 15 cm^{-1}). The DISORT model (Stamnes et al., 1988)
192 provides the most accurate radiance simulations but the runs are very time consuming. The Isaacs (Isaacs
193 et al. 1987) 2-stream algorithm is fast but oversimplified. The Scaled Isaacs method performs radiance
194 calculations using Isaacs 2-stream model over full spectral range and using DISORT model at a small
195 number of atmospheric window wavelengths. The multiple scattering contributions for each method are
196 identified and ratios of the DISORT and Isaacs methods are computed. This ratio is interpolated over the
197 full wavelength range, and finally, applied as a multiple scattering scale factor in a spectral radiance
198 calculation performed with the Isaacs method.

199 To optimize simulation speed and accuracy, we performed various sensitivity tests, including
200 combinations of multiple scattering models, band resolution, and number of streams. **Table 5** lists
201 simulation options and their corresponding calculation speed.

202 Based on results presented in **Table 5**, the efficient options (< 40 seconds) are Isaacs, DISORT 2-stream
203 with 15 cm^{-1} , DISORT 4-stream 15 cm^{-1} , and Scaled Isaacs all streams at all resolutions. Although the
204 ideal option is DISORT 8-stream with 1 cm^{-1} resolution, there is a trade-off between speed and accuracy.
205 **Fig. 6** compares DISORT simulated radiances at three band resolutions. We use two spectral ranges of
206 $0.4 - 0.5 \text{ }\mu\text{m}$ and $1.5 - 2.0 \text{ }\mu\text{m}$ to illustrate differences. **Fig. 6** shows that the coarser band resolution has
207 smoothed out the radiance variations. The 15 cm^{-1} has the smoothest curve among the three, and 1 cm^{-1}
208 shows more variations than the other two. Another (scientific) criteria for selecting the spectral resolution
209 is the ability to resolve/match the relative spectral response function (SRF) of a sensor. For example, the
210 SRFs of channels 1-6 of ABI are given at every 1 cm^{-1} .

211 Accordingly, we have chosen the 1 cm^{-1} band model for the MODTRAN radiance simulations. Performed
212 were also radiance simulations from different multiple scattering models at 1 cm^{-1} resolution. The whole
213 spectrum of $0.2 - 4 \text{ }\mu\text{m}$ was separated to 14 sections so that the differences can be assessed clearly. For
214 wavelength below $0.3 \text{ }\mu\text{m}$ and beyond 2.5 no discernible differences were found among Isaacs, DISORT
215 2-, 4-, and 8-stream, and Scaled Isaac. The largest differences occurred in the spectral range of $0.4 - 1.0$
216 μm . Scaled Isaac 8-stream follows DISORT 8-stream closely across the whole spectral range; the Scaled
217 Isaac method provided near-DISORT accuracy with the speed of Isaacs. Thus, the MODTRAN4.3
218 simulations for GOES-R ABI were set-up with Scaled Isaac 8-stream with 1 cm^{-1} band resolution.

219 For illustration, in **Fig. 7** compared are radiances simulated by Isaac 2 stream, Scaled Isaac, and DISORT-
220 4 stream for the case of Relative Azimuthal Angle= 1.9° , View Angle= 76.3° , Solar Zenith Angle= 87.2° .
221 The lines are differences between various settings and DISORT-8 stream (e.g. Isaacs minus DISORT-8).
222 Isaac has the least accuracy since it is oversimplified, 4-stream showed some improvements when
223 compared with Isaac while still has large differences for $0.4 \text{ }\mu\text{m}$ and is still computationally demanding.
224 Scaled Isaac provides the smallest differences between DISORT-8. **Fig. 7** (lower) zoomed in to the large
225 difference area of $0.3-0.35 \text{ }\mu\text{m}$ which indicates that Scaled Isaacs still provides satisfactory results.

226
227
228

2.6 Regression methodologies

We have derived coefficients of regression using a constrained least-square curve fitting methods of Matlab, “lsqnonneg”, which can solve a linear or nonlinear least-squares (data-fitting) problem and produce non-negative coefficients. Non-negative coefficients avoid generating negative TOA flux, which is not a physically valid.

To ensure that information from all channels is used and avoid the complex cross-correlation problem, it was opted to generate Narrow to Broad (NTB) coefficients for each ABI channel separately. These channel specific NTB coefficients are applied to each channel to convert ABI narrow-band reflectance to extended band. The final broad-band TOA reflectance is taken as the weighted sum of all 6-channel specific broad-band reflectance. The logic behind this approach is the assumption that the narrow-band reflectance from each channel is a good representative for a limited spectral region centered around the channel and the total spectral reflectance is dominated by the spectral region that contains the most solar energy.

To generate “separate-channel” NTB coefficients, each narrow-band ABI channel reflectance is converted to a reflectance $\rho_{bb,i}$ separately,

$$\rho_{bb,i}(\theta_0, \theta, \phi) = c_{0,i}(\theta_0, \theta, \phi) + c_{1,i}(\theta_0, \theta, \phi) * \rho_{nb,i}(\theta_0, \theta, \phi) \quad (4)$$

where $\rho_{bb,i}$ is the band reflectance for an interval around each channel i ; $c_{0,i}$ and $c_{1,i}$ are regression coefficients for channel i . These regression coefficients are derived separately for various combination of surface, cloud and aerosol types. The total shortwave broad band (0.25 – 4.0 μ m) reflectance ρ_{bb}^{est} is obtained by taking the weighted sum of all 6 $\rho_{bb,i}$ reflectance

$$\rho_{bb}^{est}(\theta_0, \theta, \phi) = \sum_i \rho_{bb,i}(\theta_0, \theta, \phi) \frac{S_{0,i}}{S_0} \quad (5)$$

Here, S_0 and $S_{0,i}$ are total solar irradiance and band solar irradiance for each channel, respectively. Band edges around the six ABI channels are: 49980-18723, 18723-13185, 13185-9221, 9221-6812, 6812-5292, 2500 cm^{-1} 0.2001-0.5341, 0.5341-0.7584, 0.7584-1.0845, 1.0845-1.4680, 1.4680-1.8896, 1.8896-4.0000 μ m). The corresponding solar irradiance band values are 364, 360, 287, 168, 91, 87

255 W m^{-2} . **Fig. 8** shows the sensor response function (SRF) and locations of the six ABI channels.
256 Coefficients are generated for clear condition and 3 types of cloudy conditions. Comparison between ABI
257 TOA flux and CERES products are shown in **Fig. 9**. The “separate-channel” coefficients work well for
258 predominantly clear sky (**Fig.10**). Differences are somewhat more scattered for cloudy cases. The reason
259 may be due to the fact that the ABI observation time and CERES product time do not match perfectly
260 since cloud condition change quickly. As discussed in Gristey et al. (2019) there are SW spectral
261 reflectance variations for different cloud types. Possibly, for ABI bands some spectral variations
262 associated with cloud variability are missed. It is important to have the correct cloud properties to be able
263 to select correct ADM. Misclassification of cloud properties will therefore result in flux differences. They
264 also argue that ADMs have an uncertainty due to within-scene variability and within-angular bin
265 variability leading to additional flux differences.

266

267 **3. Data used**

268

269 **3.1 Satellite data for GOES-16 and GOES-17**

270

271 The Advanced Baseline Imager (ABI) data used (Table 6) were downloaded from the NOAA
272 Comprehensive Large Array-Data Stewardship System (CLASS) at
273 <https://www.avl.class.noaa.gov/saa/products/welcome>. Both level 1b (L1b) and level 2 (L2) data were
274 used. These can be found by searching the CLASS site by selecting "GOES-R Series ABI Products
275 GRABIPRD (partially restricted L1b and L2+ Data Products)". The L1b data included the radiances
276 (RadC) in files “OR_ABI-L1b-RadC-MmCnn_G1SS_stime_etime_ctime, where “m”, “nn” and “SS”
277 indicate the ABI scan mode, channel number (01-06) and satellite identification number (16 or 17),
278 respectively. “stime”, and “etime” are the start and end dates and times of the scan, “ctime” is the date
279 and time the file was created. The ABI L2 product used were the clear-sky mask, cloud top phase, cloud
280 optical depth. The names of these files are constructed similarly to the L1b radiance files, except that the
281 radiance product name RadC is replaced by APMC, ACTPC, CODC and AODC, respectively, and the

282 reference to the channel number is omitted. For example, GOES-16 with ABI operating in scan mode 6
283 in the CONUS domain, the name of the clear-sky mask file is OR_ABI-L2-ACMC-M6_G16_
284 stime_etime_ctime. (In the product names above the letter C indicates the CONUS domain.)

285 The clear-sky mask product consists of a binary cloud mask identifying pixels as clear, probably clear,
286 cloudy or probably cloudy. The cloud top phase product provides cloud classification identification
287 information for each pixel. The cloud phase categories are clear sky, liquid water, super cooled liquid
288 water, mixed phase, ice, and unknown. The cloud optical depth product gives the optical thickness along
289 an atmospheric column for each pixel. All products have a nominal sub-satellite spatial resolution of 2
290 km.

291

292 When searching the NOAA CLASS site, go to "GOES-R Series ABI Products GRABIPRD (partially
293 restricted L1b and L2+ Data Products)". The SRF are downloaded from
294 <https://ncc.nesdis.noaa.gov/GOESR/ABI.php>.

295

296 **3.2 Reference data from CERES**

297

298 The CERES Single Scanner Footprint (SSF) is a unique product for studying the role of clouds, aerosols,
299 and radiation in climate. Each CERES footprint (nadir resolution 20-km equivalent diameter) on the SSF
300 includes reflected shortwave (SW), emitted longwave (LW) and window (WN) radiances and top-of-
301 atmosphere (TOA) fluxes from CERES with temporally and spatially coincident imager-based radiances,
302 cloud properties, and aerosols, and meteorological information from a fixed 4-dimensional analysis
303 provided by the Global Modeling and Assimilation Office (GMAO). Each file in this data product
304 contains one hour of full and partial-Earth view measurements or footprints at a surface reference level.
305 Detailed information can be found via <https://ceres.larc.nasa.gov/data/#ssf-level-2> (we used version 4a)
306 Near real-time CERES fluxes and clouds in the SSF format are available within about a week of
307 observation (Kratz et al., 2014). They do not use the most recent CERES instrument calibration and thus

308 contains some uncertainty. Before GOES data were transferred to the Comprehensive Large Array-data
309 Stewardship System (CLASS) system, the NOAA/STAR archive was holding new data for about a week.
310 Therefore, the initial evaluations had to be done only with data that overlapped in time. The CERES data
311 known as the FLASHFlux Level2 (FLASH_SSF) are available almost in real time from:

312 <https://ceres.larc.nasa.gov/products.php?product=FLASHFlux-Level2> (we used version 3c).

313 Due to such constraints the early comparison was done between ABI data as archived at NOAA/STAR
314 and the FLASHFlux products (in this paper, the FLASHFlux data were used only in Fig. 9). The archiving
315 of GOES-R at the NOAA Comprehensive Large Array-data Stewardship System (CLASS) started only
316 in 2019, however, it contains data starting from 2017. Once the CLASS archive became available, we
317 have augmented GOES-16 cases with observations from GOES-17; only those cases will be shown in this
318 paper.

319

320 **3.3 Data preparation**

321

322 For the re-mapping, we adopted the ESMF re-gridding package. The detailed information can be found
323 at: <http://earthsystemmodeling.org/regrid/>

324 For an ideal situation, the ABI high-resolution TOA SW fluxes should be mapped into the CERES
325 footprint for validation. However, there are reasons that make it difficult to do so. There can be more than
326 18000 pixels in a single swath of the SSF, when constrained to U.S. Different pixels have different times.
327 Neglecting the seconds, there are still more than 30 mins differences (this changes case by case) between

328 the first pixel and the one at the end and this brings up a time matching issue. By remapping the SSF to
329 ABI, we can set up a unique time for ABI (ABI is at 5 min intervals) and then constrain the region and
330 the time range of SSF.

331 Both re-mapping the ABI to SSF and remapping SSF to the ABI bring up spatial matching errors as
332 recognized by the scientific community (Rilee and Kuo, 2018; Ragulapati et al., 2021). In **Fig. 11**, we
333 show the SSF before re-gridding (**Figs 11 (a) & (b)**) and after re-gridding (**Figs. 11 (c) and (d)**). The
334 fluxes after re-mapping CERES SSF to the ABI resolution resemble well the original structure. Another
335 consideration is the computational efficiency of re-mapping the curvilinear tripolar grid to unconstructed
336 grid. For large arrays, it is more efficient to remap the unconstructed grid to the curvilinear tripolar grid.

337

338 **4. Results**

339

340 **4.1 Comparison between ABI TOA fluxes to those from CERES SSF**

341

342 A case for 2019/12/26 (doy 360) UTC 19:36 is illustrated in **Figs. 11-14**. Statistical summaries from an
343 extended number of cases that cover all four seasons are presented in **Table 7**.

344 We have conducted several experiments to select an appropriate regression approach to the NTB
345 transformation ensuring that non-physical results are not encountered. Based on the samples used in this
346 study (**Table 7**) the differences found for Terra and GOES-16 were in the range of -0.5-(-17.37) for bias
347 and 43.28-81.72 for standard deviation; for Terra and GOES-17 they were 11.26-47.09 and 70.25-108.73,
348 respectively. For Aqua and GOES-16 they were 7.63-33.87 and 58.68-117.43 respectively while for Aqua
349 and GOES-17 they were 0.19-31.53 and 47.55-129.42, respectively (all units are $W m^{-2}$). The evaluation
350 process revealed the challenges in undertaking such comparisons. Both estimates of TOA fluxes (CERES

351 and GOES) do not account for seasonality in the land use classification; the time matching for the different
352 satellites is important and limits the number of samples that can be used in the comparison. Based on the
353 results of this study recommendation for future work include the need to incorporate seasonality in land
354 use and spectral characteristic of the various surface types. Possible stratification by season in the
355 regressions could also be explored.

356 357 **4.2 Causes for differences between ABI and CERES TOA fluxes**

358 359 **4.2.1 Differences in surface spectral reflectance**

360
361 In the MODTRAN simulations we use the spectral reflectance information on various surface types as
362 provided by MODTRAN. MODTRAN version 4.3.1 contains a collection of spectral surface reflectance
363 dataset from the Moderate Spectral Atmospheric Radiance and Transmittance (MOSART) model
364 (Cornette et al., 1994) and others from Johns Hopkins University Spectral Library (Baldrige et al., 2009).
365 When doing simulation, we call the built-in surface types and use the provided surface reflectance. As
366 such, the spectral dependence of the surface reflectance used in the simulations and matched to the
367 CERES surface types may not be compatible with the classification of CERES. Also, seasonal changes
368 in surface type classification can introduce errors due to changes in the spectral surface reflectance for
369 different surface types (**Fig. 15**).

370 371 **4.2.2 Issues related to surface classification**

372
373 Another possible cause for differences between the TOA fluxes is the classification of surface types as
374 originally identified by the IGBP and used in the simulations. No seasonality is incorporated in the surface
375 type classification while such variability is part of the CERES observations.

378

379

380 **4.2.3 Issues related to match-up between GOES-R and CERES**

381

382 Both Terra and Aqua have sun-synchronous, near-polar circular orbits. Terra is timed to cross the equator
383 from north to south (descending node) at approximately 10:30 am local time. Aqua is timed to cross the
384 equator from south to north (ascending node) at approximately 1:30 pm local time. The periods for Terra
385 and Aqua are 99 and 98 minutes, respectively. Both have 16 orbits per day. CERES on Terra and Aqua
386 optical FOV at nadir is 16 x 32 or 20 km resolution. Terra passes CONUS during 03-06 UTC (US night
387 time), 16-20 UTC (US day time), and Aqua passes CONUS during 07-11 UTC (US night time), 18-22
388 UTC (US day time).

389 Both Terra and Aqua have an instantaneous FOV values at SWATH level. There is no perfect overlap,
390 temporally or spatially with ABI data. The ABI radiance and cloud data are on a regular grid of 2*2 km
391 over CONUS at each hour. To use CERES data for evaluation of ABI, there is a need to perform
392 collocation in both time and space.

393

394 **5. Summary**

395

396 The derivation and evaluation of TOA radiative fluxes as simulated for any given instrument are quite
397 challenging. In principle, there is a need to account for all possible changes in the atmospheric and surface
398 conditions one may encounter in the future. Yet, to know what these conditions are at the time of actual
399 observation when there is a need to select the appropriate combination of variables from the simulations,
400 is a formidable task. Differences in assumed cloud properties can also lead to differences in the fluxes
401 derived from the two instruments. Therefore, error can be expected due to discrepancies between the
402 actual conditions and the selected simulations and these are difficult to estimate. The approach we have
403 selected is based on high-quality simulations using a proven and accepted radiative transfer code
404 (MODTRAN) of known configurations and a wide range of atmospheric conditions. We have also

405 selected the best available estimates of TOA radiative fluxes from independent sources for evaluation.
406 However, the matching between different satellites in space and time is challenging. In selecting the cases
407 for evaluation, we have adhered to strict criteria of time and space coincidence as described in section
408 3.3.

409 Critical elements of an inference scheme for TOA radiative flux estimates from satellite observations are:

410 1) transformation of narrowband quantities into broadband ones;
411 2) transformation of bi-directional reflectance into albedo by applying Angular Distribution Models
412 (ADMs). In principle, the order in which these transformations are executed is arbitrary. However, since
413 well established, observation-based broadband ADMs derived from the Clouds and the Earth's Radiant
414 Energy System (CERES) project already exist, the logical procedure is to do the NTB transformation on
415 the radiances first, and then apply the ADM. This is the sequence that has been followed here. While the
416 road map to accomplish above objectives seems well defined, reaching the final goal of having a stable
417 up-to-date procedure for deriving TOA radiative fluxes from a new instrument like the ABI on the new
418 generation of GOES satellites is quite complicated. Since the final configuration of the instrument
419 becomes known at a much later stages the evaluation of new algorithms is in a fluid stage for a long time
420 so early evaluation against "ground truth" needs to be repeated frequently. Additional complication is
421 related to the lack of maturity of basic information needed in the implementation process, such as a
422 reliable cloud screened product which in itself is in a process of development and modifications. The
423 "ground truth", namely, the CERES observations are also undergoing adjustments and recalibration. As
424 such, the process of deriving best possible estimates of TOA radiative fluxes from ABI underwent
425 numerous iterations to reach its current status. An effort was made to deal the best way possible with the
426 fluid situation. All the evaluations against CERES were repeated once the ABI data reached stability and
427 were archived in CLASS and we used the most recent auxiliary information. This study sets the stage for
428 future possible improvements. One example is land classification which currently is static. Another issue
429 is related to the representation of real time aerosol optical properties which are important under clear sky
430 conditions. It is believed that only now when NOAA/STAR has a stable aerosol retrieval algorithm, it
431 would be timely to address the aerosol issue in the estimation of TOA fluxes under clear sky.

432 Data availability. The data are available upon request from the corresponding author.

433 Author contributions. The investigation and conceptualization were carried out by RTP, IL and JD. YM
434 and WC developed the software. RTP prepared the original draft. All authors contributed to the writing,
435 editing and review of the publication.

436 Competing interests. The authors declare that they have no conflict of interest.

437 Disclaimer. Publisher's note: Copernicus Publications remains neutral with regard to jurisdictional claims
438 in published maps and institutional affiliations.

439 Acknowledgements. We acknowledge the benefit from the use of the numerous data sources used in this
440 study. These include the Clouds and the Earth's Radiant Energy System (CERES) teams, the Fast
441 Longwave and Shortwave Radiative Flux (FLASHFlux) teams, the
442 University of Wisconsin-Madison, Space Science and Engineering Center, Cooperative Institute for
443 Meteorological Satellite Studies (CIMSS) for providing the SeeBor Version 5.0 data
444 (https://cimss.ssec.wisc.edu/training_data/), and the final versions of the GOES Imager data were
445 downloaded from <https://www.bou.class.noaa.gov/>. Several individuals have been involved in the early
446 stages of the project whose contribution led to the refinements of the methodologies. These include M.
447 M. Wonsick and Shuyan Liu. We thank the anonymous Reviewers for a very thorough and constructive
448 comments that helped to improve the manuscript. We thank the Editor Sebastian Schmidt for overseeing
449 the disposition of the manuscript.

450

451 Financial support. This research was supported by NOAA/NESDIS GOES-R Program under grants
452 5275562 1RPRP_DASR and 275562 RPRP_DASR_20 to the University of Maryland.

453

454

455 **Reference:**

- 456 Akkermans T., and Clerbaux, N.: Narrowband-to-Broadband Conversions for Top-of-Atmosphere
457 Reflectance from the Advanced Very High-Resolution Radiometer (AVHRR),
458 Remote Sens. 12 (2), 305; <https://doi.org/10.3390/rs12020305>, 2020.
- 459 Berk, A., Bernstein, L. W., and Robertson, D. C.: MODTRAN: A moderate resolution model for
460 LOWTRAN 7, Philips Laboratory, Report AFGL-TR-83-0187, Hanscom AFB, MA, 1985.
- 461 Berk, A., G. P. Anderson, P. K., Acharya, D. C. Robertson, J. H. Chetwynd, S. M. Adler-Golden:
462 MODTRAN Cloud and Multiple Scattering Upgrades with Application to AVIRIS, Remote Sensing
463 of Environment, 65 (3), 367-375, [https://doi.org/10.1016/S0034-4257\(98\)00045-5](https://doi.org/10.1016/S0034-4257(98)00045-5), 1998.
- 464 Baldridge, A. M., Hook, S. J., Grove, C. I., Rivera, G.: The ASTER spectral library version 2, Remote
465 Sensing of Environment 113, doi: 10.1016/j.rse.2008.11.007, 2009.
- 466 Borbas, E. E., Seemann, S. W., Huang, H.-L., Li, J., and Menzel, W. P.: Global profile training database
467 for satellite regression retrievals with estimates of skin temperature and emissivity. Proceedings of
468 the XIV, International ATOVS Study Conference, Beijing, China, University of Wisconsin-
469 Madison, Space Science and Engineering Center, Cooperative Institute for Meteorological Satellite
470 Studies (CIMSS), Madison, WI, pp.763-770, 2005.
- 471 Clerbaux, N., Russell, J. E., Dewitte, S., Bertrand, C., Caprion, D., De Paepe, B., Sotelino, L. G., Ipe, A.,
472 Bantges, R., and Brindley, H. E.: Comparison of GERB instantaneous radiance and flux products
473 with CERES Edition-2 data, Rem. Sens. of Environ., **113**, 102-114. doi:
474 10.1016/j.rse.2008.08.016, 2009.
- 475 Cornette, W. M., Acharya, P. K., Robertson, D. C., and Anderson, G. P.: Moderate Spectral Atmospheric
476 Radiance and Transmittance Code (*MOSART*), Rep. R-057-94 (11–30), La Jolla, CA: Photon
477 Research Associates, 1994.
- 478 Gristey, J. J., Su, W., Loeb, N. G., Vonder Haar, T. H., Tornow, F., Schmidt, K. S., Hakuba, M. Z.,

479 Pilewskie, P., Russell, J. E.: Shortwave Radiance to Irradiance Conversion for Earth Radiation
480 Budget Satellite Observations: A Review, *Remote Sens.* 13, 2640,
481 <https://doi.org/10.3390/rs13132640>, 2021.

482 Kato, S., Loeb, N. G., Rutan, D. A., Rose, F. G.: Clouds and the Earth's Radiant Energy System
483 (CERES) Data Products for Climate Research *Journal of the Meteorological Society of Japan*,
484 93 (6), 597–612, DOI:10.2151/jmsj.2015-048, 2015.

485 Kratz, D. P., Stackhouse Jr., P. W., Gupta, S. K., Wilber, A. C., Sawaengphokhai, P., and McGarragh, G.
486 R.: The Fast Longwave and Shortwave Flux (FLASHFlux) Data Product: Single-Scanner Footprint
487 Fluxes, *J. Appl. Meteor. Climatology*, 53, 1059-1079, doi: 10.1175/JAMC-D-13-061.1, 2014.

488 Hansen, M. C., Defries, R. S., Townshend, J. R. G., and Sohlberg, R.: Global land cover classification
489 at 1km spatial resolution using a classification tree approach, *International Journal of Remote*
490 *Sensing*, 21(6-7):1331 – 1364, DOI:10.1080/014311600210209
491 <https://doi.org/10.1080/014311600210209>, 2010.

492 Harries, J. E., Russell, J. E., Hanafin, J. A., Brindley, H., Futyan, J., Rufus, J., Kellock, S., G. Matthews,
493 R. Wrigley, A. Last, J. Mueller, R. Mossavati, J. Ashmall, E. Sawyer, D. Parker, M. Caldwell, P
494 M. Allan, A. Smith, M. J. Bates, B. Coan, B. C. Stewart, D. R. Lepine, L. A. Cornwall, D. R.
495 Corney, M. J. Ricketts, D. Drummond, D. Smart, R. Cutler, S. Dewitte, N. Clerbaux, L. Gonzalez,
496 A. Ipe, C. Bertrand, A. Joukoff, D. Crommelynck, N. Nelms, D. T. Llewellyn-Jones, G. Butcher,
497 G. L. Smith, Z. P. Szewczyk, P. E. Mlynchak, A. Slingo, R. P. Allan, and M. A. Ringer: The
498 Geostationary Earth Radiation Budget Project, *Bull. Amer. Meteor. Soc.* 86 (7): 945, doi:
499 10.1175/BAMS-86-7-945, 2005.

500 Isaacs, R. G., W.-C. Wang, R. D. Worsham, and S. Goldenberg, S.: Multiple scattering LOWTRAN and
501 FASCODE models. *Applied Optics*, 26(7), 1272 – 1281, 1987.

502 Kato, S., and Loeb, N. G.: Top-of-atmosphere shortwave broadband observed radiance
503 and estimated irradiance over polar regions from Clouds and the Earth's Radiant Energy System
504 (CERES) instruments on Terra, *J. Geophys. Res.*, 110, D07202,
505 doi:10.1029/2004JD005308, 2005.

506 Laszlo, I., Liu, H., Kim, H.-Y., and Pinker, R. T. : GOES-R Advanced Baseline Imager (ABI) Algorithm
507 Theoretical Basis Document (ATBD) for Downward Shortwave Radiation (Surface), and Reflected
508 Shortwave Radiation (TOA), version 3.1, Available at <https://www.goes-r.gov/resources/docs.html>,
509 2018.

510 Laszlo, I., Liu, H., Kim, H.-Y., and Pinker, R. T.: Shortwave Radiation from ABI on the GOES-R Series,
511 in: *The GOES-R Series*, edited by S. J. Goodman, T. J. Schmit, J. Daniels and R. J. Redmon. 179-191,
512 Elsevier, doi: <https://doi.org/10.1016/B978-0-12-814327-8.00015-9>, 2020.

513 Loeb, N. G., Smith, N. M., Kato, S., Miller, W. F., Gupta, S. K., Minnis, P. and Wielicki, B. A.: Angular
514 Distribution Models for Top-of Atmosphere Radiative Flux Estimation from the Mission Satellite,
515 Part I: Methodology, *Journal of Applied Meteorology*, 42 240-265, 2003.

516 Loeb N. G. et al.: Angular distribution models for top-of- atmosphere radiative flux estimation from the
517 Clouds and the Earth's Radiant Energy System Instrument on the Terra satellite. part I:
518 Methodology. *J. Atmos. Oceanic Technol.*, 22:338–351, 2005.

519 Loveland T. R., B. C. Reed, J. F. Brown, D. O. Ohlen, Z. Zhu, L. Yang, J. W. Merchant: Development
520 of a global land cover characteristics database and IGBP DISCover from 1 km AVHRR data,
521 *International Journal of Remote Sensing*, 21 (6-7), 1303-1330, 2010.

522 Ma, Y., R. T. Pinker, M. M. Wonsick, C. Li, and L. M. Hinkelman: Shortwave radiative fluxes on
523 slopes. *JAMC*, 55, 1513-1532, <https://doi.org/10.1175/JAMC-D-15-0178.1>, 2016.

524 Ma, Y. and Pinker, R. T.: Shortwave Radiative Fluxes from Satellites: An Update. *J. Geophys. Res.*
525 *Atmos.*, 117, Issue D23, DOI: 10.1029/2012JD018332, 2012.

526 Niu, X. and Pinker, R. T.: Revisiting satellite radiative flux computations at the top
527 of the atmosphere, *International Journal of Remote Sensing*, DOI:10.1080/01431161.2011.571298,
528 2011.

529 Niu, X. and Pinker, R. T.: An improved methodology for deriving high resolution
530 surface shortwave radiative fluxes from MODIS in the Arctic region, *J. Geophys. Res.*
531 *Atmos.*, 120, 2382–2393, doi: 10.1002/2014JD022151, 2015.

532 Pinker, R. T., Zhang B., Dutton E. G.: Do satellites detect trends in surface solar radiation? *SCIENCE*,
533 308, 5723, 850-854, 2005.

534 Pinker, R. T., A. Bentamy, B. Zhang, W. Chen, and Ma, Y.: The net energy budget at the ocean-
535 atmosphere interface of the “Cold Tongue” region, *J. Geophys. Res. Oceans*, 122, doi: 10.1002/
536 2016JC012581, 2017a.

537 Pinker, R. T., S. Grodsky, B. Zhang, A. Busalacchi, and Chen, W.: ENSO Impact on Surface Radiative
538 Fluxes as Observed from Space. *J. Geophys. Res.-Oceans.*, doi: 10.1002/2017JC012900, 2017b.

539 Pinker, R. T., Zhang, B. Z., Weller, R. A., and Chen, W.: Evaluating surface radiation fluxes observed
540 from satellites in the southeastern Pacific Ocean. *Geophysical Research Letters*, 45.
541 <https://doi.org/10.1002/2017GL076805>, 2018.

542 Rajulapati, C. R., S. M. Papalexiou, M. P. Clark, and Pomeroy, J. W.: The Perils of Regridding:
543 Examples Using a Global Precipitation Dataset, *Journal of Applied Meteorology and*
544 *Climatology*, 60 (11), 1561–1573, doi: 10.1175/JAMC-D-20-0259.1, 2021.

545 Rilee M. L. and Kuo, K. S.: The Impact on Quality and Uncertainty of Regridding Diverse Earth
546 Science Data for Integrative Analysis, IN43C-0916, 2018.

547 Scarino et al.: A Web-Based Tool for Calculating Spectral Band Difference Adjustment Factors Derived
548 from SCIAMACHY Hyperspectral Data, *IEEE Trans. Geo. Remote Sens.*, 54, 5,
549 10.1109/TGRS.2015.2502904, 2016.

550 Stamnes, K., S.-C. Tsay, W. Wiscombe and K. Jayaweera: Numerically stable algorithm for discrete-
551 ordinate-method radiative transfer in multiple scattering and emitting layered media, *Applied*
552 *Optics*, 27 (12), 2502–2509, 1988.

553 Su, W., Corbett, J., Eitzen, Z., and Liang, L.: Next-generation angular distribution models for
554 top-of-atmosphere radiative flux calculation from CERES instruments: methodology, *Atmos.*
555 *Meas. Tech.*, 8, 611–632, <https://doi.org/10.5194/amt-8-611-2015>, 2015.

556 Wang, H; Pinker, R. T.: Shortwave radiative fluxes from MODIS: Model development and
557 implementation. *JGR- Atmospheres*, 114, D20201, 2009.

558 Wielicki, B. A.; Doelling, D. R.; Young, D. F.; Loeb, N. G.; Garber, D. P.; MacDonnell, D. G.: Climate
559 quality broadband and narrowband solar reflected radiance calibration between sensors in orbit.
560 In Proceedings of the IGARSS 2008 IEEE International Geoscience and Remote Sensing
561 Symposium, Boston, MA, USA, 7–11 July 2008.

562 Zhang, T., Stackhouse Jr., P. W., Cox, S. J., Mikovitz, J. C., Long, C. N.: Clear-sky shortwave
563 downward flux at the Earth's surface: Ground-based data vs. satellite-based data, *Journal of*
564 *Quantitative Spectroscopy & Radiative Transfer*, 224, 247-260, 2019,
565 www.elsevier.com/locate/jqsrt.

566
567
568
569

Tables

Table 1. Channel information and spectral bands for ABI.

<i>ABI Band #</i>	<i>Central wavelength (μm)</i>	<i>Spectral band (μm)</i>
1	VIS 0.47	0.45-0.49
2	VIS 0.64	0.60-0.68
3	NIR 0.86	0.847-0.882
4	NIR 1.38	1.366-1.380
5	NIR 1.61	1.59-1.63
6	NIR 2.26	2.22-2.27

570

571

572

573 Table 2. Surface classification description for IGBP 18 types, IGBP 12 types, CERES clear sky 6 types,
 574 and NTB cloudy sky 4 types

IGBP (18 types)	IGBP (12 types)	CERES clear-sky (6 types)	NTB cloudy-sky (4 types)
Evergreen Needleleaf	Needleleaf Forest	Mod-High Tree/Shrub	Land
Deciduous Needleleaf			
Evergreen Broadleaf	Broadleaf Forest		
Deciduous Broadleaf			
Mixed Forest	Mixed Forest		
Closed Shrublands	Closed Shrub		
Woody Savannas	Woody Savannas		
Savannas	Savannas		
Grasslands	Grasslands		
Permanent Wetlands			
Tundra			
Croplands		Croplands	
Open Shrublands	Open Shrub		
Urban and Built-up	Open Shrub	Dark Desert	Desert
Bare Soil and Rocks	Barren and Desert	Bright Desert	
Snow and Ice	Snow and Ice	Snow and Ice	Snow and Ice
Water Bodies	Ocean	Ocean	Water

575

576

577

578

579 Table 3. The various classes for which NTB coefficients are generated.

Parameter	Clear condition	Cloudy condition
Aerosol or cloud type	6 aerosol types (rural, maritime, urban, tropospheric, fog, desert)	3 cloud types (cirrus, stratocumulus, altostratus)
Optical depth (OD)	Typical VIS (km) values for each aerosol types (no OD grid for each aerosol type). Rural: 23, maritime: 23, urban: 5, tropospheric: 50, fog: 0.2, desert: (default VIS for wind speed 10m/s)	Cirrus: [0, 0.8, 1.2, 1.8, 3.2] Stratocumulus: [0, 0.8, 1.2, 1.8, 3.2, 5.8, 8.2, 15.8, 32.2, 51.8, 124.2] Altostratus: [0, 15.0, 30.0, 50.0, 80.0]
Surface type	12 IGBP surface types	4 types (Water, Land, Desert, Snow/Ice)

580

581

582

583

584 Table 4. Angles used in simulations. To be consistent with what is presented in the

585 ABI Shortwave Radiation Budget (SRB) Algorithm Theoretical Basis Documents (ATBD) (Laszlo

586 et al, 2018) the additional angles used in the simulations are not given in this Table.

Angle Type	Angles
Solar Zenith Angle [°]	0.0, 12.9, 30.8, 41.2, 48.3, 56.5, 63.2, 69.5, 75.5, 81.4, 87.2
Satellite Zenith Angle [°]	0.0, 11.4, 26.1, 40.3, 53.8, 65.9, 76.3
Azimuth Angle [°]	0.0, 1.9, 10.0, 24.2, 44.0, 68.8, 97.6, 129.3, 162.9, 180

587

588

589

590

591

Table 5. MODTRAN simulation speed test (CPU MHz 2099.929).

Algorithm	Stream	Band Resolution (cm ⁻¹)	Speed (~seconds)
Isaacs	2	1	40
DISORT	2	1, 5, 15	280, 70, 30
	4	1, 5, 15	560, 120, 40
	8	1, 5, 15	930, 300, 110
Scaled Isaac	2	1, 5, 15	30, 10, 6.67
	4	1, 5, 15	30, 10, 6.67
	8	1, 5, 15	30, 10, 6.67

592

593

594

595

596 Table 6. Details on data used as input for calculations.

597

Short Name	Long Name	MODE	ABI-Channel	Scan Sector	Spatial Resolution
RadC	L1b Radiance	M6	C01-C06	CONUS	5000x3000
AODC	L2 Aerosol	M6	--	CONUS	2500x1500
ACMC	L2 Clear Sky Masks	M6	--	CONUS	2500x1500
ACTPC	L2 Cloud Top Phase	M6	--	CONUS	2500x1500
CODC*	L2 Cloud Optical Depth	M6	--	CONUS	2500x1500

598

599 *The CODC data were not always available from CLASS and had to be obtained from NOAA/STAR
600 temporary archives. Also, not all the required angular information needed for implementation of the
601 regressions is available online and had to be re-generated.

602

603

604 Table 7. Statistical summary for all selected cases inter-compared at instantaneous time scale.

Case	CERES	GOES-R	Corr	Bias	Std	RMSE	N
07/31 2019	Terra	G16	0.82	0.81	69.81	69.81	0.22 x10 ⁶
		G17	0.87	29.13	90.10	94.70	1.78 x10 ⁶
UTC 19	Aqua	G16	0.76	33.87	117.43	122.22	1.58 x10 ⁶
		G17	0.78	31.53	129.42	133.21	0.29 x10 ⁶
09/13 2019	Terra	G16	0.87	-17.37	81.72	83.54	0.13x10 ⁶
		G17	0.71	47.09	108.73	118.48	1.73x10 ⁶
UTC 20	Aqua	G16	0.76	18.22	108.50	110.02	1.46x10 ⁶
		G17	0.73	25.14	81.95	85.72	0.53x10 ⁶
09/21 2019	Terra	G16	0.85	6.78	66.66	67.00	0.35x10 ⁶
		G17	0.83	26.41	87.64	91.57	1.75x10 ⁶
UTC 19	Aqua	G16	0.82	29.66	105.09	109.20	1.67x10 ⁶
		G17	0.76	6.03	94.70	94.89	0.15x10 ⁶
09/30 2019	Terra	G16	0.88	4.49	64.79	64.94	0.40x10 ⁶
		G17	0.80	19.35	86.41	88.55	1.74x10 ⁶
UTC 19	Aqua	G16	0.80	19.87	100.45	102.40	1.69x10 ⁶
		G17	0.72	2.71	91.79	91.83	0.12x10 ⁶
	Terra	G16	0.86	5.84	51.44	51.77	0.35x10 ⁶

10/23		G17	0.87	22.47	70.25	73.76	1.75x10 ⁶
2019		G16	0.89	17.10	75.95	77.85	1.67x10 ⁶
UTC	Aqua	G17	0.78	8.98	72.52	73.07	0.15x10 ⁶
19		G16	0.87	-0.50	43.28	43.28	0.35x10 ⁶
11/08	Terra	G17	0.82	17.18	71.27	73.31	1.75x10 ⁶
2019		G16	0.90	10.08	71.27	71.98	1.67x10 ⁶
UTC	Aqua	G17	0.68	1.53	47.55	47.58	0.15x10 ⁶
19		G16	0.79	7.98	49.10	49.75	0.35x10 ⁶
11/24	Terra	G17	0.87	14.10	78.35	79.61	1.76x10 ⁶
2019		G16	0.82	7.63	58.68	59.17	1.67x10 ⁶
UTC	Aqua	G17	0.65	0.19	63.14	63.14	0.15x10 ⁶
19		G16	0.88	5.24	53.28	53.54	0.35x10 ⁶
12/26	Terra	G17	0.76	11.26	73.95	74.80	1.76x10 ⁶
2019		G16	0.83	9.79	58.90	59.56	1.67x10 ⁶
UTC 19	Aqua	G17	0.73	0.85	52.53	52.54	0.15x10 ⁶

605
606
607
608
609
610
611
612
613

614 List of Figures

- 615 Figure 1. Flowchart of the NTB transformations illustrating the main processing sections.
- 616 Figure 2. Schematic illustration of the logic employed to synthesize modeled and observed ADMs.
- 617 Figure 3. The location of the 100 selected clear sky profiles from SeeBor used in the simulations.
- 618 Figure 4. Profile statistics of: (a) temperature; (b): water vapor; (c) ozone for the entire available sample
619 and for the reduced sample used in this study. Error bar is 1 standard deviation.
- 620 Figure 5. Re-mapped IGBP surface classifications over the CONUS at 2-km ABI grid.
- 621 Figure 6. Simulated Radiances from DISORT 8-stream (with 1, 5, and 15 cm^{-1} resolution band model
622 for spectral range of 0.4 – 0.5 μm (left) and 1.5 – 2.0 μm (right).
- 623 Figure 7. Radiance differences between various multi-scattering algorithms and DISORT-8 stream.
624 *Upper*: the whole simulated spectrum of 0.2-4 μm ; *Lower*: zoom on 0.3-0.35 μm (Relative
625 Azimuthal Angle=1.9°, View Angle=76.3°, Solar Zenith Angle=87.2°).
- 626 Figure 8. Locations of the six ABI channel SRFs. X-axis is wavenumber. Y-axis is solar irradiance.
- 627 Figure 9. Comparison of TOA flux from ABI and CERES FLASHFlux for 2017/11/25, 17:57Z. (a)
628 CERES Terra product; (b): results with “separate-channel” coefficients. (c): difference (ABI-
629 CERES); (d): histogram of ABI-CERES differences (this is the only case illustrated in this paper
630 with data from FLASHFlux)
- 631 Figure 10. Statistics for relative Bias and RMSE. The y-axis is percentage. The x-axis is the case used in
632 the inter-comparison. Blue - cloudy orange - clear sky and t gray - all sky.
- 633 Figure 11. (a) All sky TOA SW from CERES_SSF/Aqua, (b) CERES_SSF/Terra, (c) re-gridded
634 CERES_SSF/Aqua, (d) re-gridded CERES_SSF/Terra, (e) GOES-16 and (f) GOES-17 on
635 12/26/2019 at UTC 19:36.
- 636 Figure 12. (a) Frequency distribution of all-sky TOA SW differences between ABI on GOES-16 and
637 CERES, (b) ABI on GOES-17 and CERES_SSF using Aqua (Upper) and Terra (Lower). All
638 observations were used (clear and cloudy) on 12/26/2019 at UTC 19:36.
- 639 Figure 13. Same as Figure 11 but for clear TOA SW differences.

640 Figure 14. Same as Figure 11 but for cloudy TOA SW differences.

641 Figure 15. *Left:* Sensor response function for ABI channel 6; *Right:* Spectral albedo for desert and open
642 shrubs. Desert albedo value is much higher than open shrubs at 2.2 μm .

643

644

645

646

647

648

649

650

651

652

653

654

655

656

657

658

659

660

661

662

663

664

665

666

667

668

669

670

671

672

673

674

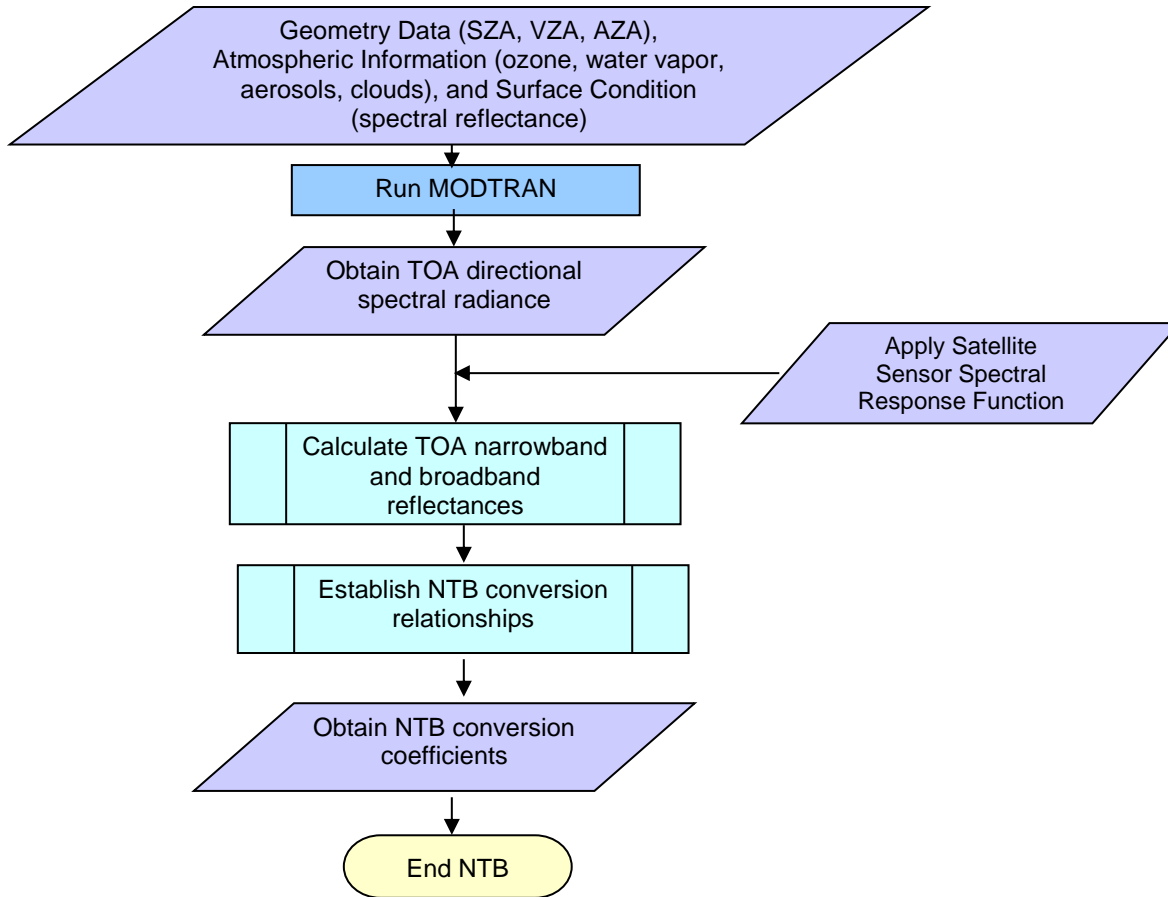
675

676

677 **Figures**

678

679



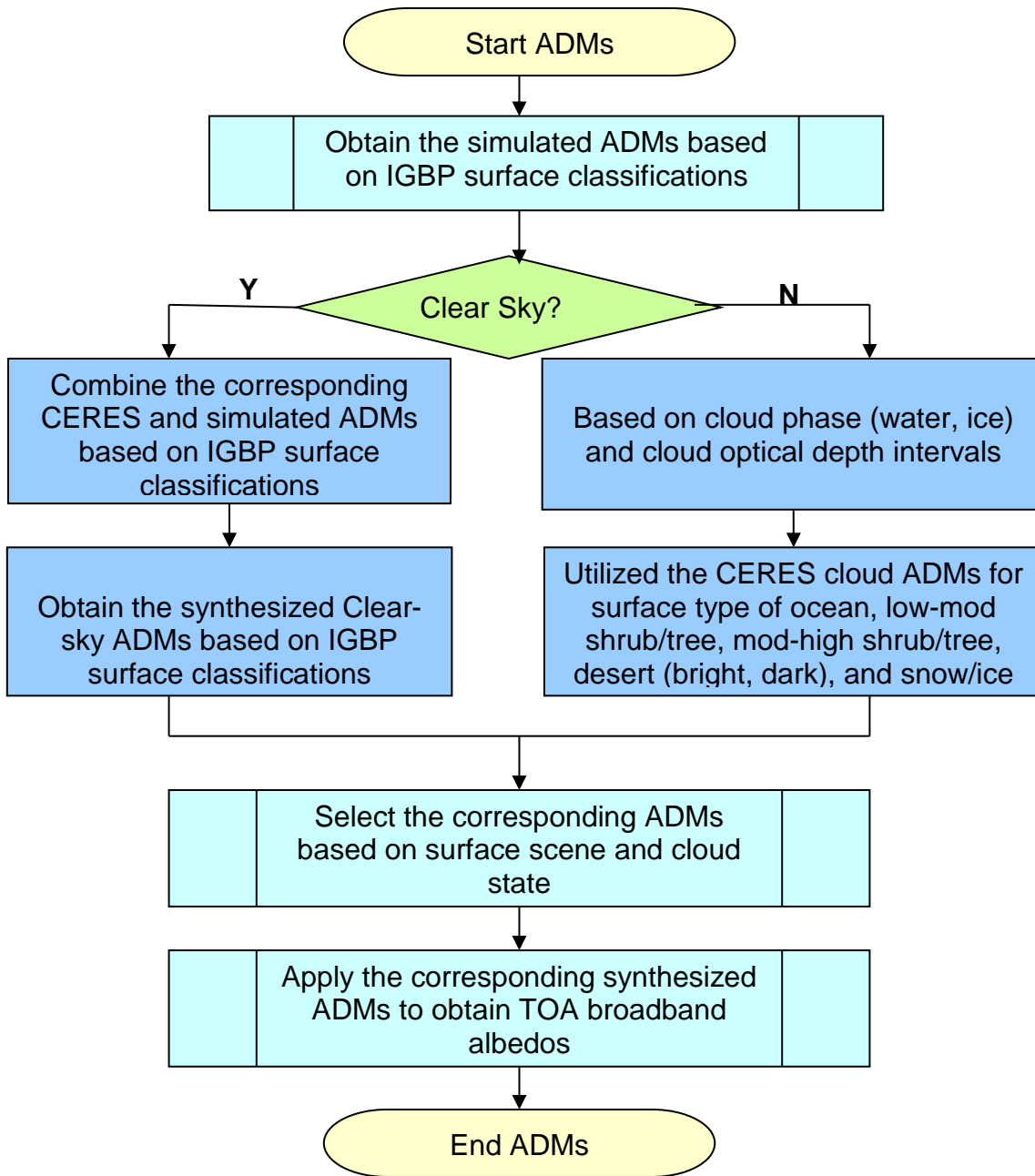
680

681 Figure 1. Flowchart of the NTB transformations illustrating the main processing sections.

682

683

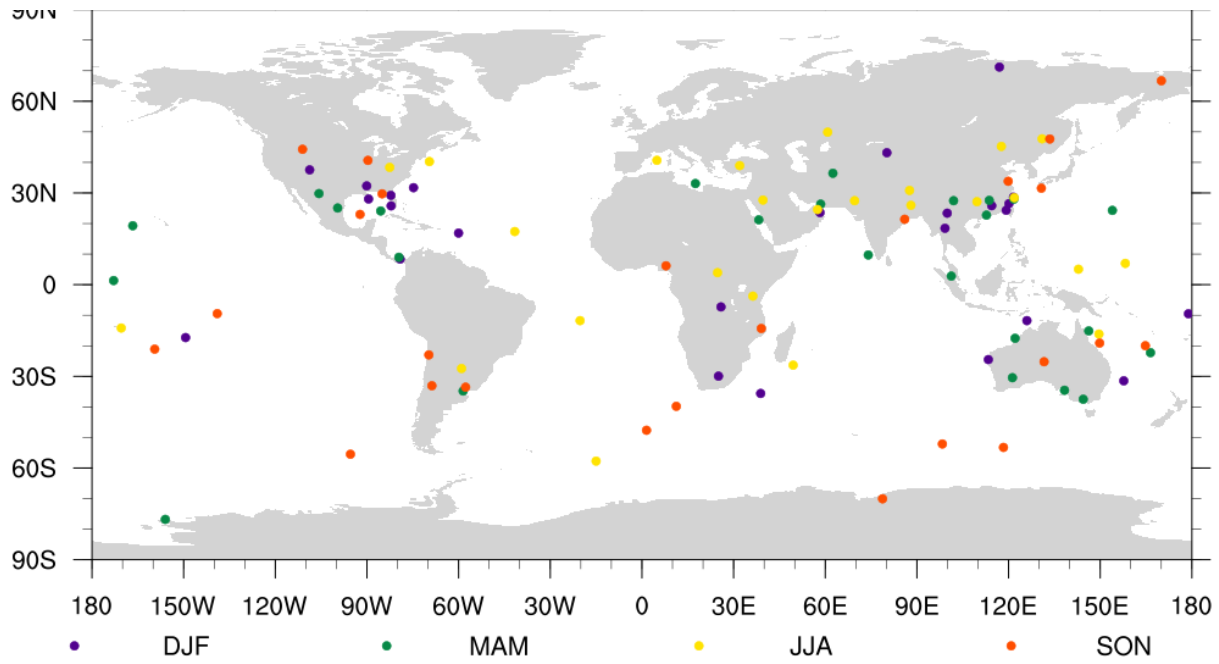
684



685

686 Figure 2. Schematic illustration of the logic employed to synthesize modeled and observed ADMs.

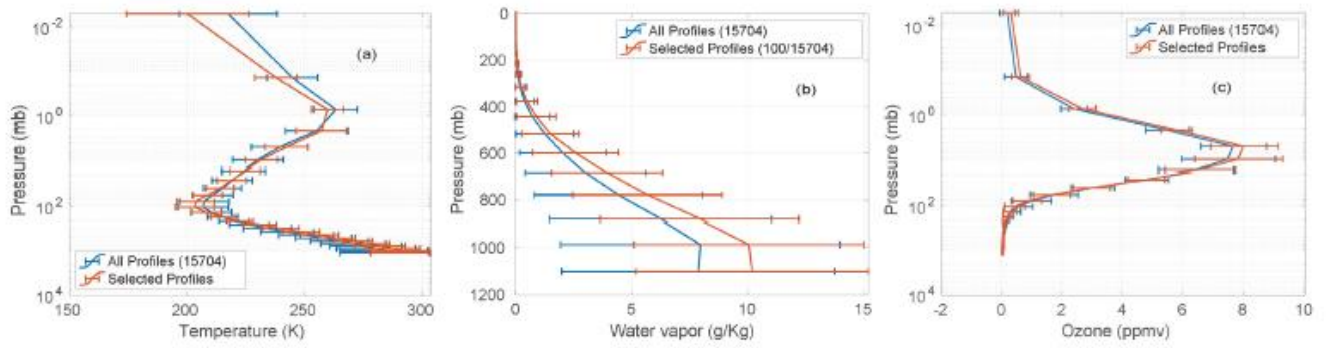
687
688
689
690



691
692
693

Figure 3. The location of the 100 selected clear sky profiles from SeeBor used in the simulations.

694

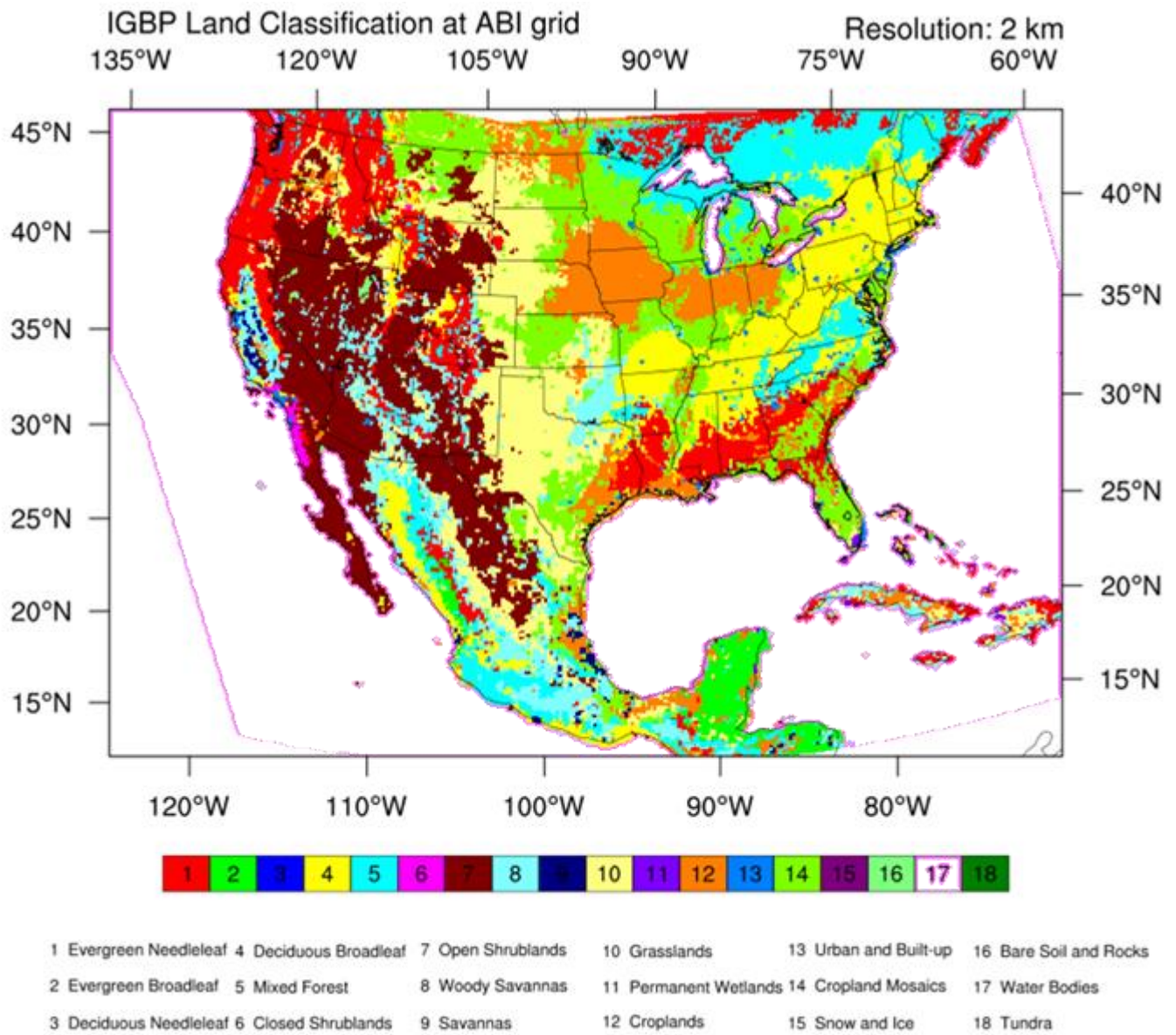


695

696 Figure 4. Profile statistics of: (a) temperature; (b) water vapor; (c) ozone for the entire available sample
697 and for the reduced sample used in this study. Error bar is 1 standard deviation.

698

699



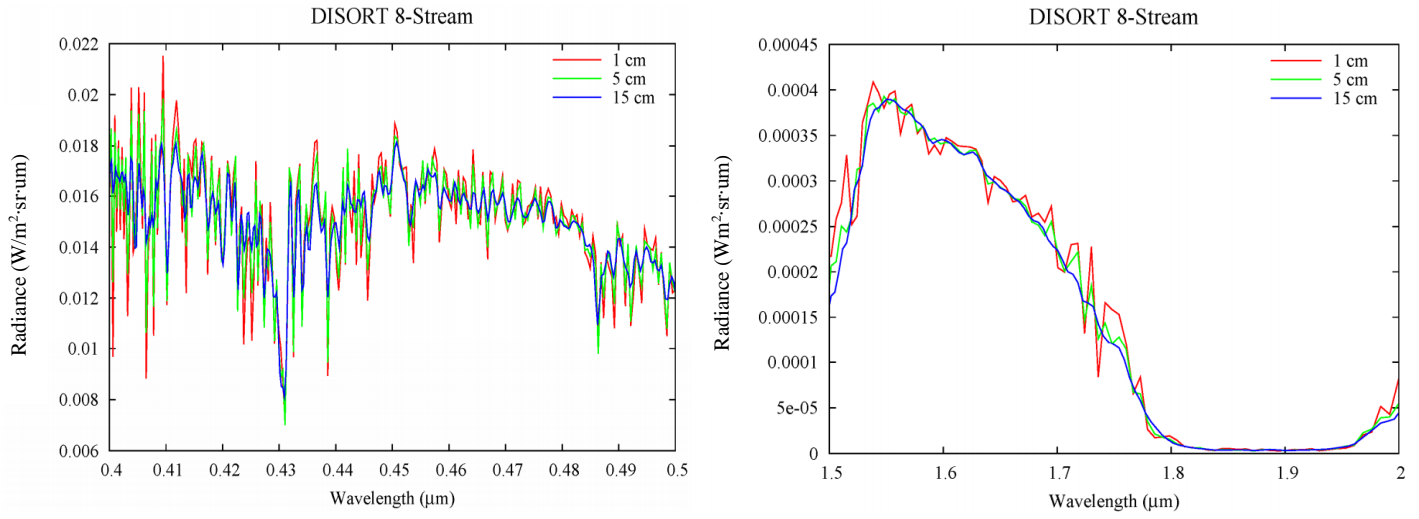
701

702 Figure 5. Re-mapped IGBP surface classifications over the CONUS at 2-km ABI grid.

703

704

705



706

707

708

709

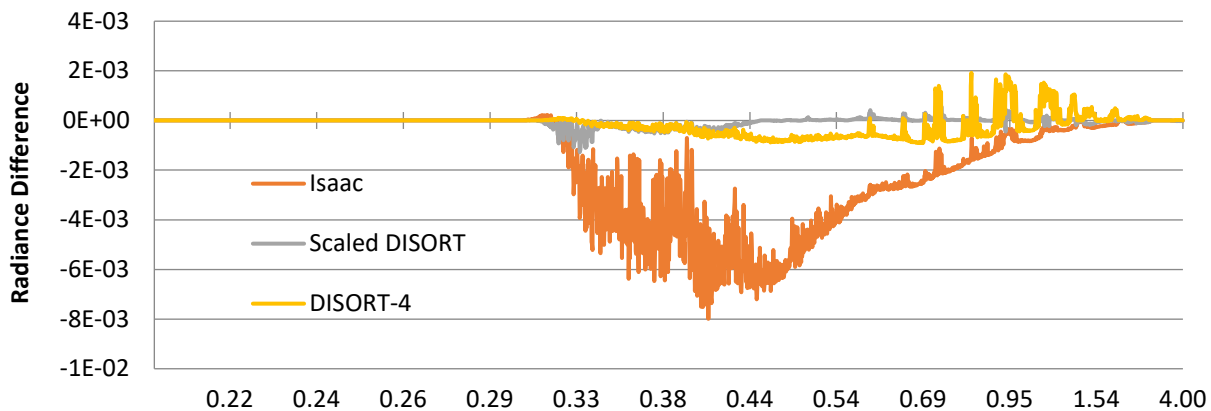
710

Figure 6. Simulated Radiances from DISORT 8-stream (with 1, 5, and 15 cm⁻¹ resolution band model for spectral range of 0.4 – 0.5 μm (left) and 1.5 – 2.0 μm (right).

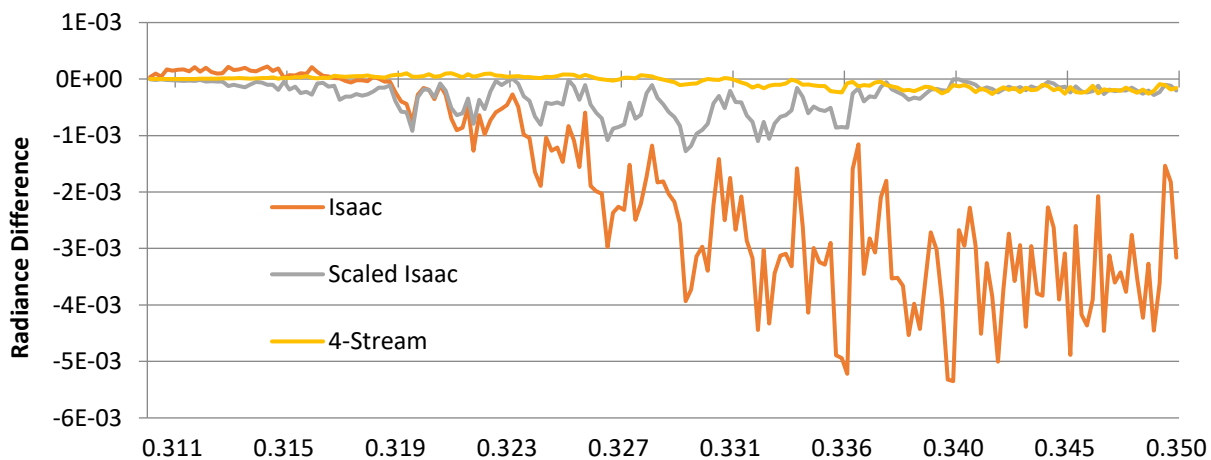
711

712

Radiance difference between multiscattering algorithms and DISORT-8 Stream



713

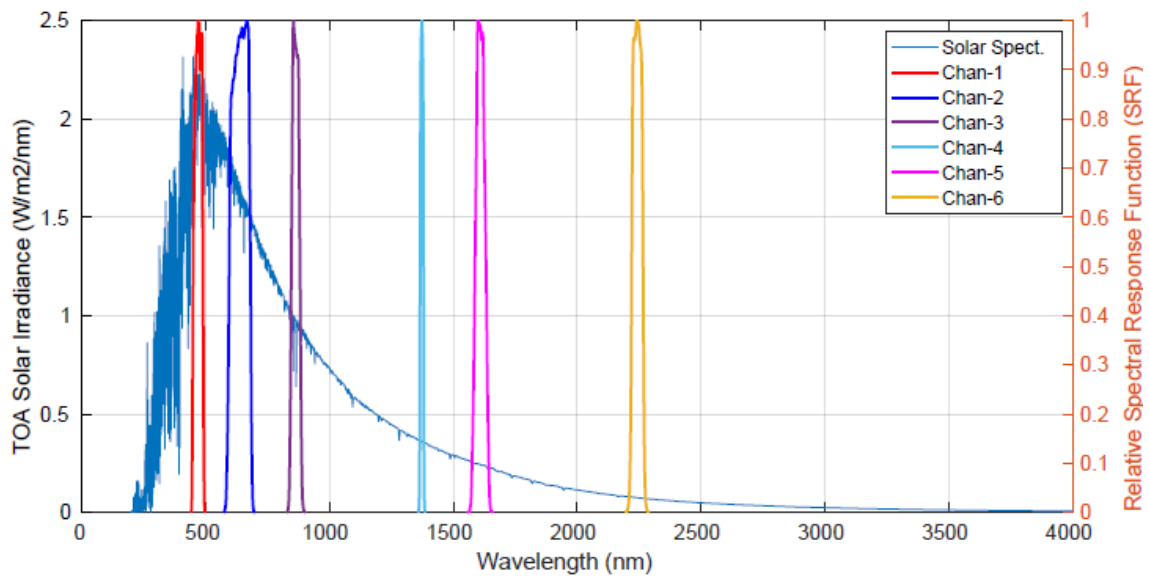


714

715 Figure 7. Radiance differences between various multi-scattering algorithms and DISORT-8 stream.

716 *Upper: the whole simulated spectrum of 0.2-4 μm ; Lower: zoom on 0.3-0.35 μm (Relative*
717 *Azimuthal Angle=1.9°, View Angle=76.3°, Solar Zenith Angle=87.2°).*

718



719

720

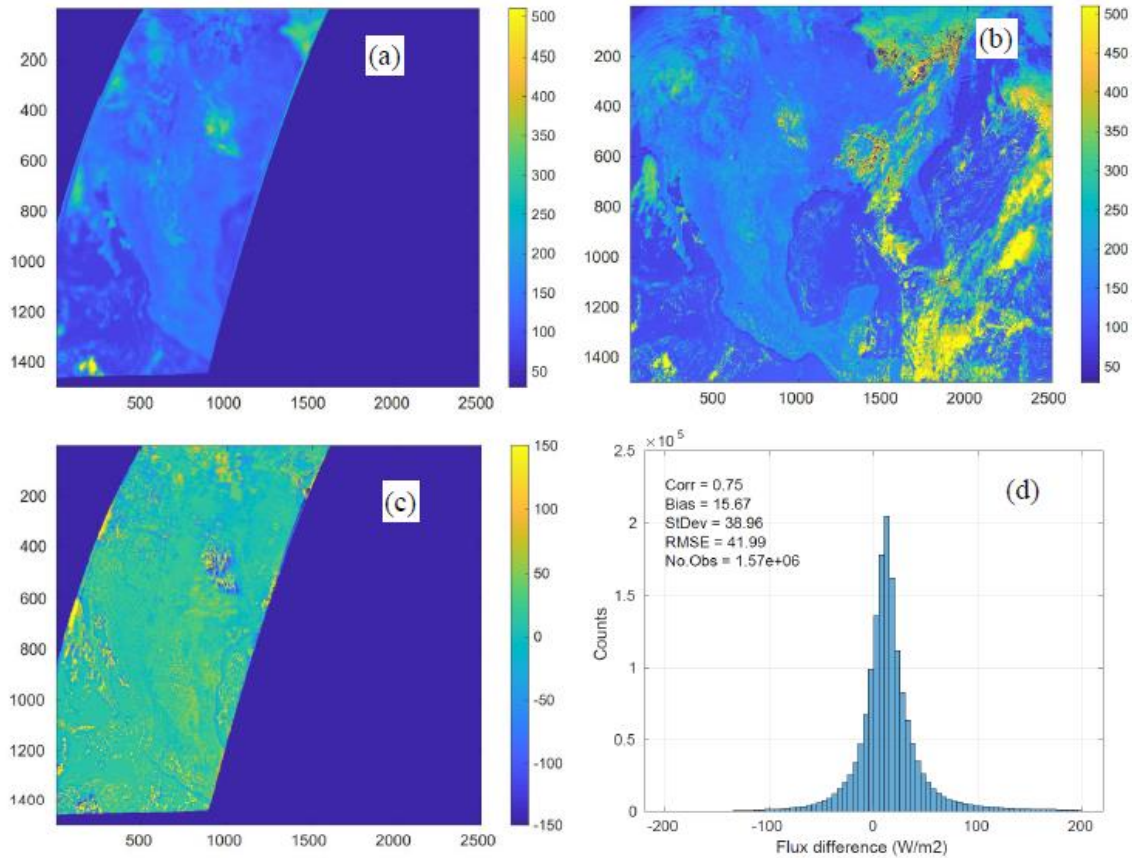
721 Figure 8. Locations of the six ABI channel SRFs. X-axis is wavenumber. Y-axis is solar irradiance.

722

723

724

725



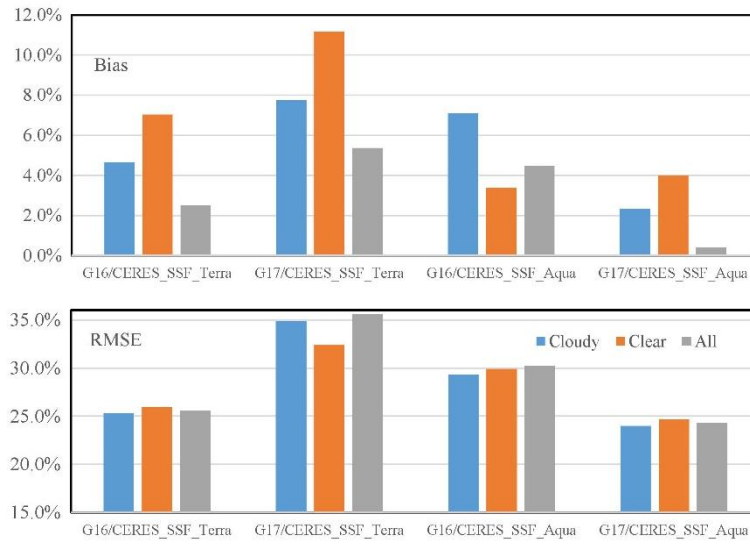
726

727 Figure 9. Comparison of TOA flux from ABI and CERES FLASHFlux for 2017/11/25, 17:57Z. (a)
 728 CERES Terra product; (b): results with “separate-channel” coefficients. (c): difference (ABI-
 729 CERES); (d): histogram of ABI-CERES differences (this is the only case illustrated in this paper
 730 with data from FLASHFlux).

731

732

733



734

735

736

Figure 10. Statistics for relative Bias and RMSE. The y-axis is percentage. The x-axis is the case used in the inter-comparison. Blue - cloudy orange - clear sky and t gray - all sky.

737

738

739

740

741

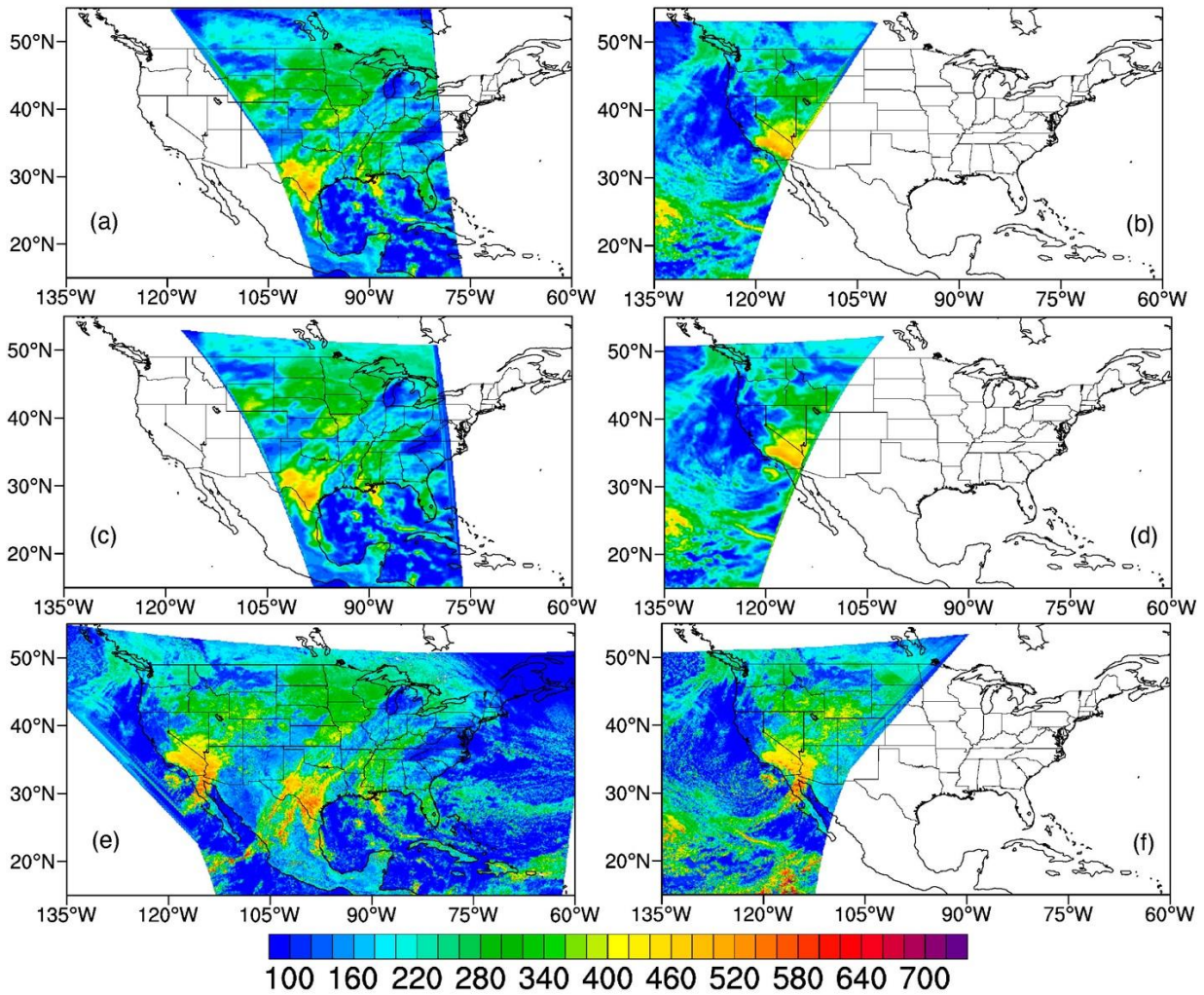
742

743

744

745

746



747
 748
 749
 750
 751
 752
 753
 754

Figure 11. (a) All sky TOA SW from CERES_SSF/Aqua, (b) CERES_SSF/Terra, (c) re-gridded CERES_SSF/Aqua, (d) re-gridded CERES_SSF/Terra, (e) GOES-16 and (f) GOES-17 on 12/26/2019 at UTC 19:36.

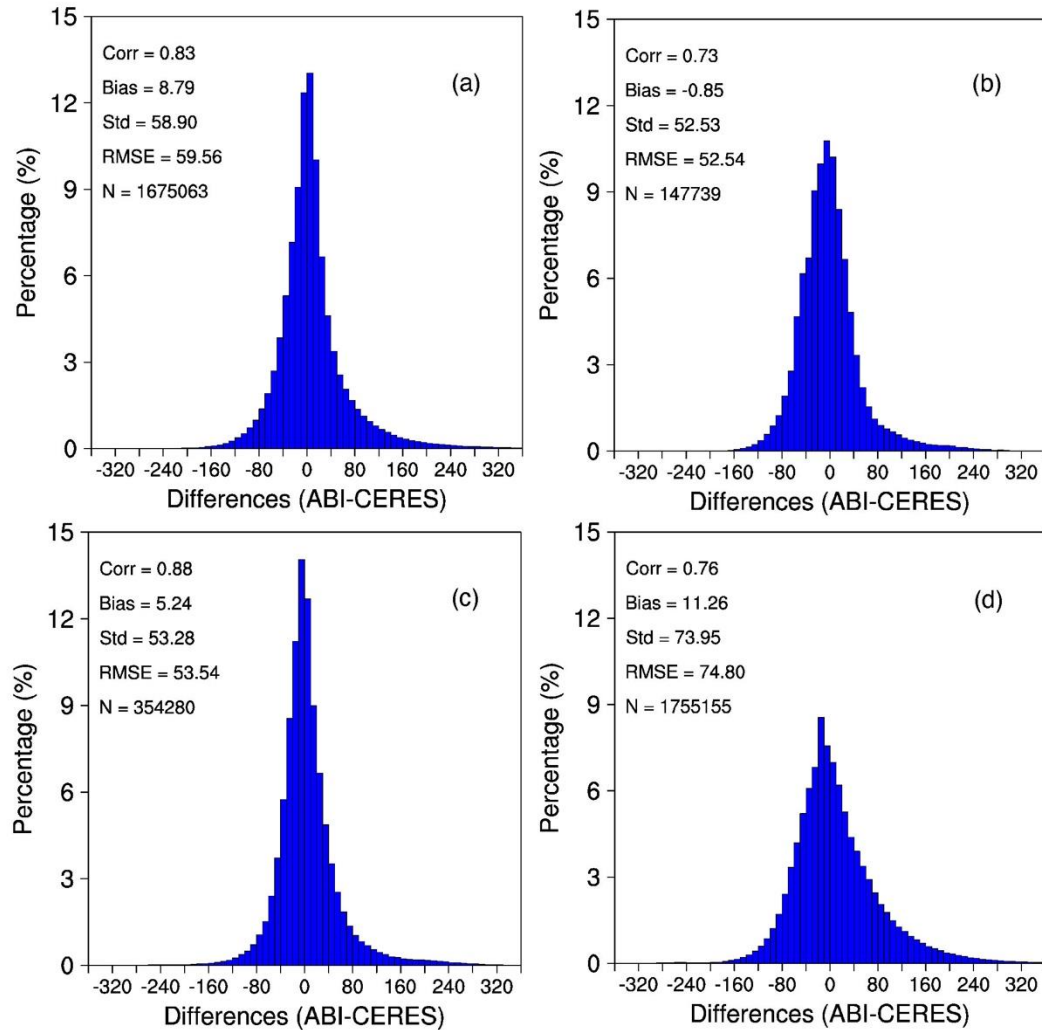


Figure 12. (a) Frequency distribution of all-sky TOA SW differences between ABI on GOES-16 and CERES, (b) ABI on GOES-17 and CERES_SSF using Aqua (Upper) and Terra (Lower). All observations were used (clear and cloudy) on 12/26/2019 at UTC 19:36.

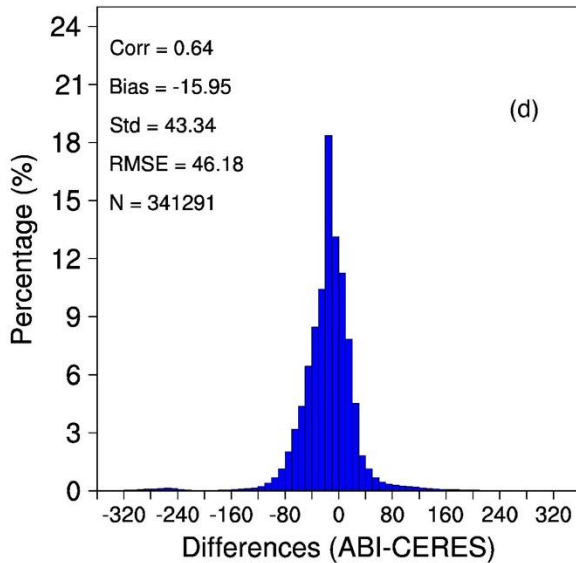
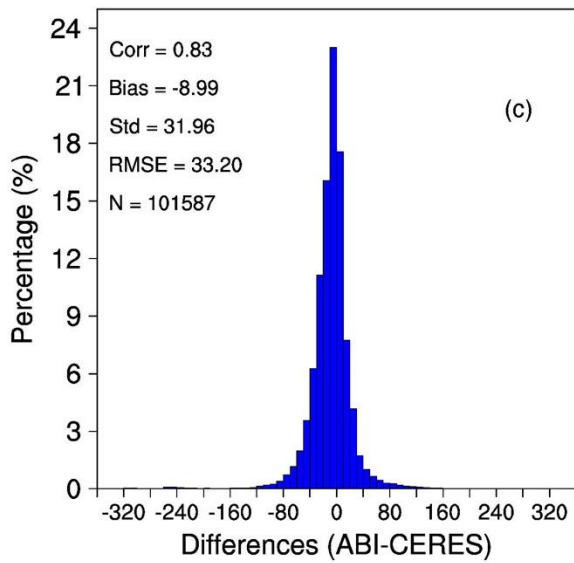
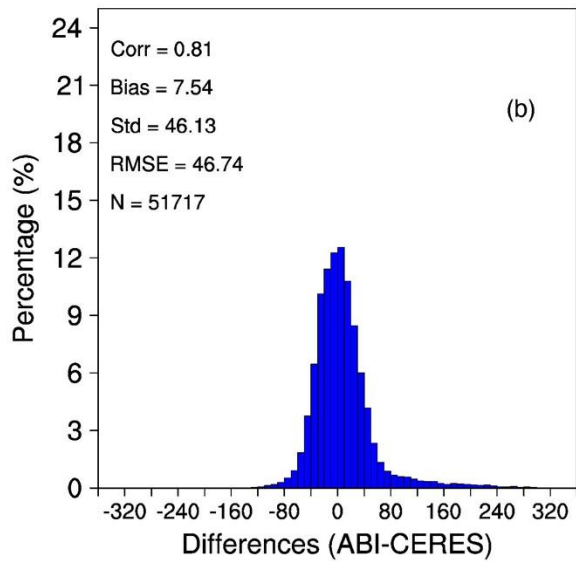
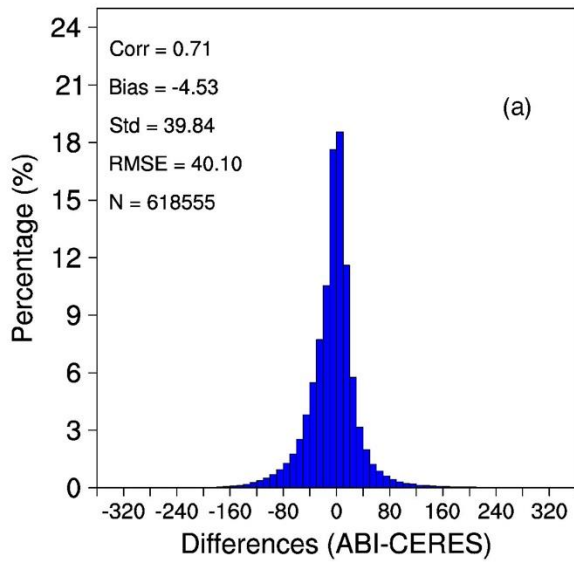
756

757

758

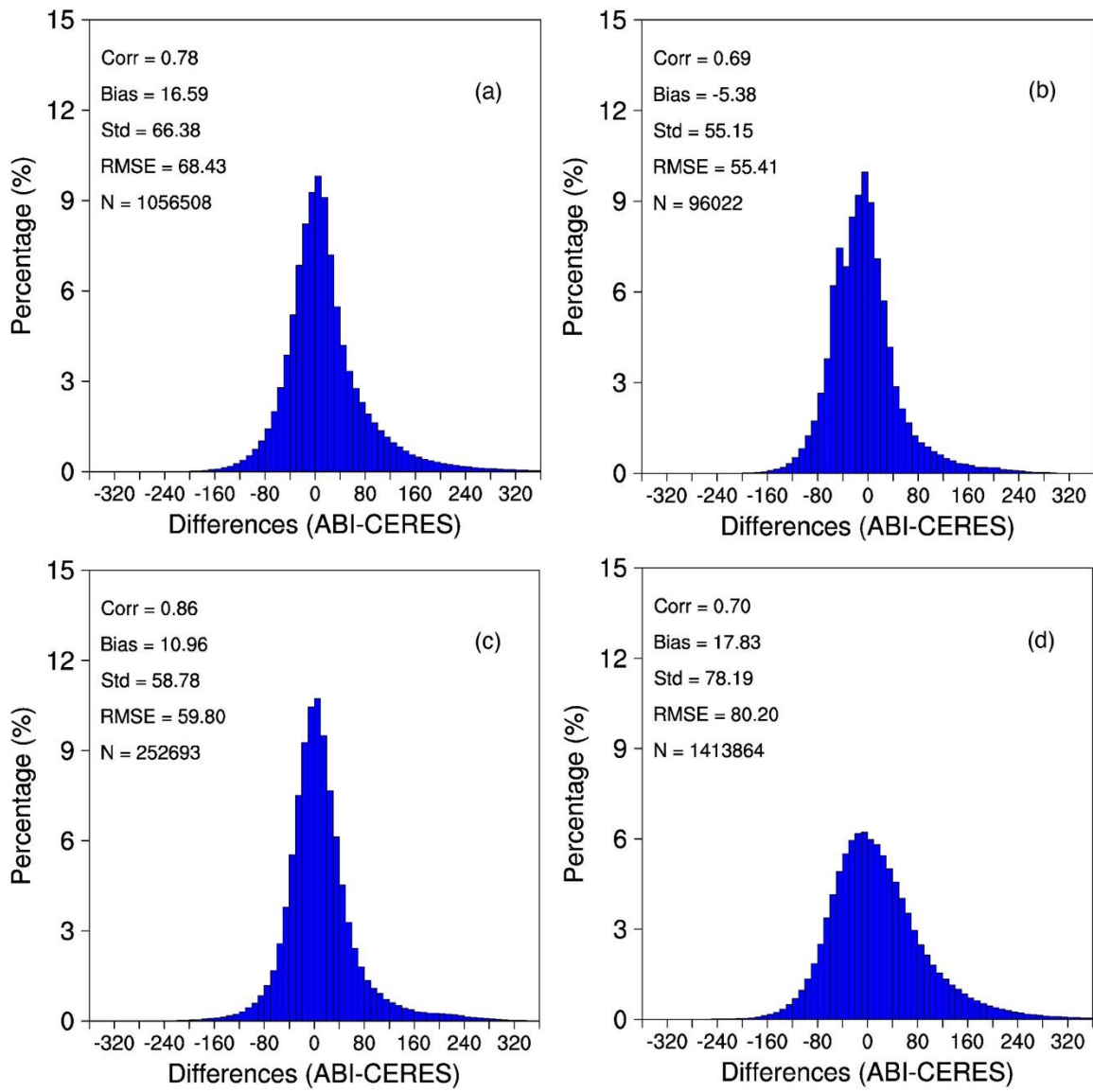
759

760



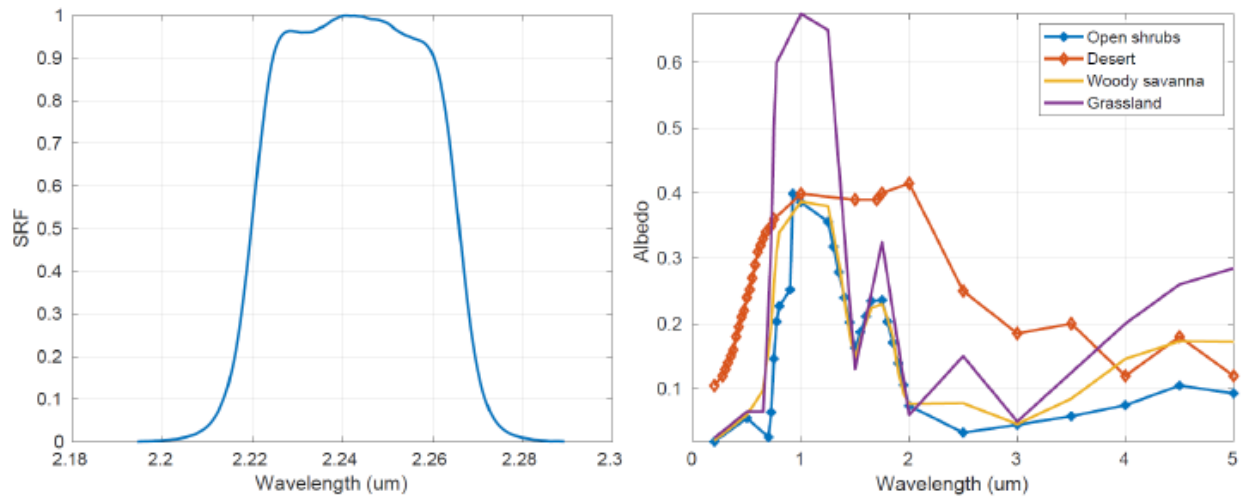
761
762
763

Figure 13. Same as Figure 11 but for clear TOA SW differences.



764
765 Figure 14. Same as Figure 11 but for cloudy TOA SW differences.

766
767



769

770 Figure 15. *Left:* Sensor response function for ABI channel 6; *Right:* Spectral albedo for desert and open
 771 shrubs. Desert albedo value is much higher than open shrubs at 2.2 μm.

772

773